Chemistry & Biology
Article

A Structural View of the Inactivation of the SARS Coronavirus Main Proteinase by Benzotriazole Esters

Koen H.G. Verschueren,[1] Ksenia Pumpor,[1] Stefan Anemüller,[1] Shuai Chen,[1] Jeroen R. Mesters,[1] and Rolf Hilgenfeld[1,*]
[1]Institute of Biochemistry, Center for Structural and Cell Biology in Medicine, University of Lübeck, Ratzeburger Allee 160, 23538 Lübeck, Germany
*Correspondence: hilgenfeld@biochem.uni-luebeck.de
DOI 10.1016/j.chembiol.2008.04.011

SUMMARY

The main proteinase (M^{pro}) of the severe acute respiratory syndrome (SARS) coronavirus is a principal target for the design of anticoronaviral compounds. Benzotriazole esters have been reported as potent nonpeptidic inhibitors of the enzyme, but their exact mechanism of action remains unclear. Here we present crystal structures of SARS-CoV M^{pro}, the active-site cysteine of which has been acylated by benzotriazole esters that act as suicide inhibitors. In one of the structures, the thioester product has been hydrolyzed and benzoic acid is observed to bind to the hydrophobic S2 pocket. This structure also features the enzyme with a shortened N-terminal segment ("amputated N finger"). The results further the understanding of the important role of the N finger for catalysis as well as the design of benzotriazole inhibitors with improved specificity.

INTRODUCTION

The global 2003 outbreak of the highly infectious severe acute respiratory syndrome (SARS) was caused by a new human coronavirus, SARS coronavirus (SARS-CoV) (Ksiazek et al., 2003; Drosten et al., 2003; Peiris et al., 2003). Spreading from southern China, the disease was responsible for the death of about 10% of those infected (Stockman et al., 2006). Since 2003 there have been two isolated mini-outbreaks in China, but they have been contained in their early stages. These cases remind us of the lingering danger to human health represented by SARS-CoV as well as other coronaviruses, and the need for effective anticoronaviral therapeutics. Since the global SARS outbreak, two new coronaviruses infecting humans have been discovered (van der Hoek et al., 2004; Fouchier et al., 2004; Woo et al., 2005). HCoV NL63, a coronavirus associated with croup (Chiu et al., 2005), appears to be the most widespread member of the entire family. It is the causative agent of up to 10% of all respiratory diseases (Pyrc et al., 2006 and references therein). Detected in 13 patients in Hong Kong, HCoV HKU1 is a coronavirus associated with relatively mild, community-acquired pneumonia characterized by fever, running nose, and cough (Lau et al., 2006), although a subtype of HKU1 causing a severe obstructive pneumonia was recently identified (Kupfer et al., 2007). Two other human coronaviruses, HCoV 229E and OC43, have been known for decades, and are believed to cause mild upper respiratory tract illnesses, including the common cold (McIntosh et al., 1967). Furthermore, HCoV OC43 has also been reported to have a high prevalence in the brains of multiple sclerosis patients (Arbour et al., 2000).

Coronaviruses are enveloped, positive-sense RNA viruses. Their large single-stranded RNA genome ranges from 27 to 31 kb (29.7 kb for SARS-CoV) and encodes several structural and auxiliary proteins as well as two large overlapping polyproteins, pp1a (replicase 1a, ~486 kDa for SARS-CoV) and pp1ab (replicase 1ab, ~790 kDa) (Thiel et al., 2003). These polyproteins are subsequently cleaved to give rise to the individual nonstructural proteins essential for building the viral replicase complex. In most coronaviruses, this maturation process is performed by extensive proteolytic processing by three cysteine peptidases. There are two papain-like proteinases (PL^{pro}) that are responsible for acting on three cleavage sites near the N terminus of the polyproteins (Ziebuhr et al., 1995), and the main proteinase or M^{pro} (also called "3C-like protease" or $3CL^{pro}$), which is necessary for cleaving at no less than 11 conserved sites containing a large hydrophobic residue (preferably Leu) in the P2 position, a Gln in the P1 position, and a small aliphatic amino acid residue (Ser, Gly, Ala) in the P1′ position (Ziebuhr et al., 2000; Hegyi and Ziebuhr, 2002; Anand et al., 2003). In contrast to other coronaviruses, the SARS-CoV genome encodes only one PL^{pro} in addition to the M^{pro}. Besides being involved in the processing of the polyproteins, the PL^{pro} has a second function as a deubiquitinating enzyme (Barretto et al., 2005; Lindner et al., 2005). Because of its pivotal role in viral replication, the 33.8 kDa main proteinase has become the prime target in the development of inhibitors directed at SARS-CoV and other coronaviruses (Anand et al., 2003, 2005).

So far, the crystal structures of the main proteinases of four coronaviruses have been determined: transmissible gastroenteritis virus (TGEV) (Anand et al., 2002), HCoV 229E (Anand et al., 2003), SARS-CoV (Yang et al., 2003; Tan et al., 2005; Xu et al., 2005; Xue et al., 2007), and infectious bronchitis virus (IBV) (Xue et al., 2008). Except for IBV, the enzyme is a homodimer, and this is the quaternary structure observed in solution as well (Anand et al., 2002; Fan et al., 2004; Hsu et al., 2005a). In fact, it has been proposed that dimerization is essential for catalytic activity because the very amino terminus ("N finger") of one subunit is involved in organizing the substrate-binding pocket of the other (Anand et al., 2002; Yang et al., 2003; Tan et al., 2005).

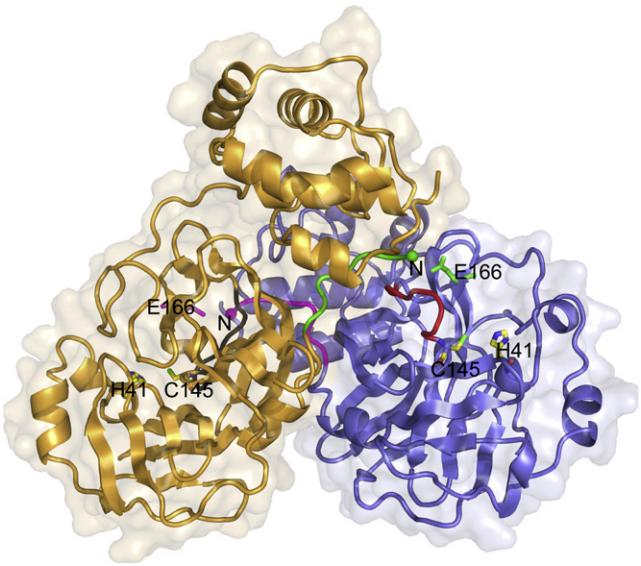

Figure 1. Dimer of the SARS CoV M^{pro}
Ribbon diagram and surface representation of the dimeric SARS-CoV M^{pro} (protomer A in blue, protomer B in light orange). The catalytic dyad residues (Cys145 and His41) in both monomers colored by atom (yellow, carbon; red, oxygen; blue, nitrogen; green, sulfur). The N finger (residues 1–7) is colored magenta for monomer A and green for monomer B. The very N terminus is marked by a sphere. It interacts with residue Glu166 of the opposing monomer. The oxyanion loop is colored red for monomer A and dark brown for monomer B.

Each monomer of the coronaviral M^{pro} consists of three domains. Domains I (residues 1–101) and II (residues 102–184) each consist of an antiparallel β barrel; taken together, domains I and II resemble the structure of chymotrypsin-like serine proteinases (Anand et al., 2002, 2003; Yang et al., 2003; Tsukada and Blow, 1985). The active site of the M^{pro} is located in the interface between the two domains and consists of a Cys-His catalytic dyad, in which the cysteine acts as the nucleophile in the proteolytic cleavage reaction (Anand et al., 2002, 2003; Yang et al., 2003). Connected by a long loop (residues 185–200) to domain II, domain III is all-helical and not only involved, to some extent, in dimer formation but also in placing the N finger next to the substrate-binding site of the other monomer. In the active conformation of the protein, the individual binding pockets for the respective amino acid residues of the substrate are accessible and the oxyanion loop (residues 138–145) has the correct shape to donate two hydrogen bonds from main-chain amides to stabilize the tetrahedral transition state of the proteolysis reaction. The two monomers in the dimer are arranged perpendicular to each other (Figure 1; Yang et al., 2003).

A number of crystal structures with small-molecule inhibitors bound to the coronavirus M^{pro} have been reported. Most of these compounds are peptide analogs derived from the substrate cleavage consensus sequence, such as peptidyl chloromethyl ketones (Anand et al., 2003; Yang et al., 2003), vinylogous alkyl ester derivatives serving as Michael acceptors (Yang et al., 2005), aza-peptide epoxides (Lee et al., 2005, 2007), or α,β-epoxiketones (Goetz et al., 2007). Peptidyl aldehydes have been described as reversible inhibitors (Al-Gharabli et al., 2006; Schmidt et al., 2008). Also, structure-based virtual screening approaches have led to the discovery of a number of nonpeptidic inhibitors (Wu et al., 2004; Bacha et al., 2004; Chen et al., 2005b; Kaeppler et al., 2005; Tsai et al., 2006), but until now, only a few crystal structures of such complexes with the protease have been reported (e.g., Lu et al., 2006).

In the early stages of the 2003 SARS outbreak, one of the first drugs tried for the treatment of patients was ribavirin, an antiviral drug commonly used against a number of DNA and RNA viruses (Sidwell et al., 1972), but this proved to be unsuccessful (Stockman et al., 2006; Knowles et al., 2003). Left with few other options, physicians also tested HIV proteinase inhibitors (Stockman et al., 2006), and Wu et al. (2006) found that one of them, lopinavir, targeted SARS-CoV M^{pro} with an IC_{50} of ≈50 μM. In their search for derivatives of lopinavir with an improved inhibitory action toward M^{pro}, Wu et al. (2006) noticed by serendipity that the intermediate benzotriazole esters occurring during the synthesis of these derivatives were better inhibitors of the enzyme than the final products (see also Hilgenfeld and Pumpor, 2006). These benzotriazole esters are the result of the activation of carboxylic acids by 2-(1*H*-benzotriazole-1-yl)-1,1,3,3-tetramethyluronium hexafluorophosphate (HBTU), which was used as a coupling reagent in the synthesis of the lopinavir-like molecules. Wu et al. (2006) reported K_i = 7.5 nM and k_{inact} (=k_3) = 0.0011 s^{-1} for the best of these inhibitors and suggested, on the basis of mass spectrometric analyses, that the benzotriazole esters irreversibly acylate the active-site Cys145. However, even though these K_i values are among the lowest for any inhibitor of the SARS-CoV M^{pro} described so far, Wu et al. (2006) also reported that full inhibition of the enzyme could not be achieved. Also, upon replacement of the ester oxygen by a methylene group, the inhibitors bound noncovalently to the enzyme, with K_i values in the micromolar range (Wu et al., 2006). Such a mechanism might also apply, to some extent, to the benzotriazole esters themselves, perhaps explaining the incomplete inhibition reported by Wu et al. (2006). Because of these uncertainties, we wanted to visualize the binding mode of benzotriazole esters to the SARS-CoV main proteinase, and have determined the crystal structures of the enzyme after incubation with two such compounds, 1-(benzoyloxy)-benzotriazole (compound XP-27) and 1-(4-dimethylaminobenzoyloxy)-benzotriazole (compound XP-59) (see Figure 2).

RESULTS AND DISCUSSION

Chain Termini of the SARS-CoV M^{pro} Influence Catalytic Activity

Two different gene constructs coding for the SARS-CoV main proteinase were used in this study. One of them ([ΔSer1]/C-His_6) has the last two residues at the C terminus of the protein (Phe305 and Gln306) replaced by a hexahistidine tag, while the codon for the N-terminal serine has been replaced by the start codon, AUG. As we can demonstrate by Edman degradation (not shown), the corresponding formylmethionine residue was cleaved off during synthesis in *Escherichia coli*, most probably by methionyl-aminopeptidase (Hirel et al., 1989), creating Δ(Ser1)/C-His_6 M^{pro}. The other construct ("authentic M^{pro}") carries an N-terminal GST-AVLQ tag that is autocleaved by the protease itself, and a C-terminal GP-H_6 tag which can be removed

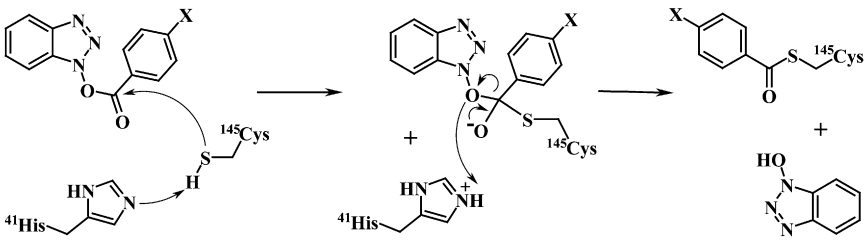

Figure 2. Chemical Formulas and Reaction Mechanism
Formulas for compounds XP-27 (X = H) and XP-59 (X = $[CH_3]_2N$) and proposed reaction mechanism (Wu et al., 2006).

by PreScission protease, so that the final proteinase product possesses the authentic N and C termini (Xue et al., 2007). The difference in enzymatic activity and dimer stability between the two constructs illustrates the importance of an intact N terminus (N finger). The k_{cat}/K_M of the (ΔSer1)/C-His_6 protein, determined by using an HPLC-based assay with the pentadecapeptide SWTSAVLQ↓SGFRKWA as a substrate, was 61.9 (±1.5) $mM^{-1}min^{-1}$ (Tan et al., 2005). Using a FRET-based assay with a fluorogenic peptide substrate (Dabcyl-KTSAVLQ↓SGFRKME-Edans), this value was 167.9 $mM^{-1}min^{-1}$. The K_D value for the monomer-dimer equilibrium of this enzyme species was estimated at ≈250 nM by using the method of Kuo et al. (2004), much lower than the values derived for a similar construct by Graziano et al. (2006) from small-angle scattering and chemical crosslinking. Accordingly, the fraction of catalytically active (ΔSer1)/C-His_6 dimers at the enzyme concentration used in the assays (1.0 μM with respect to monomers) is about 0.8, and the k_{cat}/K_M of this enzyme species has to be corrected to ≈209 $mM^{-1}min^{-1}$. The M^{pro} with the authentic chain termini, however, is significantly more active under the same circumstances and has a k_{cat}/K_M value of 502.3 $mM^{-1}min^{-1}$. For the latter enzyme, the K_D value for dimer dissociation was estimated to be significantly lower than 100 nM, in agreement with most reports in the literature (Kuo et al., 2004; Hsu et al., 2005b). This would indicate that >>90% of the authentic M^{pro} molecules exist as dimers at the concentration of 1.0 μM (with respect to monomers) used in the assays. Occasionally, much higher K_D values have been reported for SARS-CoV M^{pro} dimer dissociation in the literature (e.g., Fan et al., 2004; Chen et al., 2005a), but in most of these cases, the enzyme did not have authentic chain termini.

For the authentic enzyme, we determined K_M = 2.2 mM and k_{cat} = 1105 min^{-1}, whereas for (ΔSer1)/C-His_6, the respective values were 0.24 mM and 40.3 min^{-1} (prior to correction for dimer dissociation; see above). Thus, the authentic enzyme, although displaying a 10-fold larger K_M value, exhibited a 27-fold higher activity than (ΔSer1)/C-His_6. The crystal structures presented below provide an explanation for this observation.

Kinetic Data for the Benzotriazole Inhibitors

We found the benzotriazole derivatives to be potent inhibitors of SARS-CoV M^{pro}, capable of inhibiting half of the authentic enzyme activity at low micromolar concentrations (<5 μM and 0.1 μM for XP-27 and XP-59, respectively), as determined using the fluorogenic peptide cleavage assay. Under the assumption that the inhibitors act as suicide substrates by covalently binding to the proteinase, a description of the compounds requires determination of both the equilibrium binding constant K_i and the inactivation rate constant (for covalent bond formation) k_3 (=k_{inact}), according to the following scheme (Scheme I, Equation VIII.127 of Dixon and Webb, 1979):

$$\begin{array}{ccc} & K_i \quad k_3 & \\ E & \leftrightarrows\ EI \rightarrow & E\text{-}I \\ K_s & \downarrow\uparrow & \\ & ES & \end{array}$$

In competition with the fluorescent peptide substrate (S), the inhibitor initially forms a Michaelis complex with the proteinase, which subsequently undergoes a nucleophilic attack by Cys145 onto the ester bond, leading to the formation of a covalent enzyme-inhibitor product (see Figure 2 for chemical formulas and reaction mechanism). The leaving group of the reaction is 1-hydroxybenzotriazole. For the inhibitor XP-59, the K_i and k_3 values were determined as 1.38 μM and 0.013 s^{-1}, respectively. At an inhibitor concentration of 1.3 μM, approximately 97% inhibition of the enzyme was achieved. For the inhibitor XP-27, the exact determination of the inhibition constant proved difficult because of the inherent instability of this compound. UV absorption of XP-27 decreased in anhydrous dimethyl sulfoxide (DMSO) over time, even in the absence of enzyme, and this process was significantly enhanced by addition of a few microliters of water. Addition of XP-27 to the enzyme led to rapid inactivation, but after about 3–4 min, the enzyme activity started to recover (Figure 3A). A possible reason for this behavior is that the rather instable thioester product may have been partially hydrolyzed. As we shall see below, our crystal structure of the enzyme acylated by XP-27 provides an explanation for this observation. In contrast to XP-27 and its thioester product with the enzyme, XP-59 and its covalent M^{pro} adduct were more stable, because the electron-donating nature of the p-dimethylamino group decreased the electrophilicity of the carbonyl C atom. The inhibition curve (fluorescence versus time) of XP-59 displayed the expected hyperbolic shape (Figure 3B).

Wu et al. (2006) reported a K_i value of 17.4 nM and a k_3 of 0.0013 s^{-1} for XP-59 (their compound 4). We have no immediate explanation for the discrepancy by a factor of 80 between the K_i value reported by these authors and our findings, nor for the factor of 10 between their and our k_3 values. We also do not know whether the k_{cat}/K_M value of their enzyme preparation is comparable to ours.

Binding of 1-(Benzoyloxy)-Benzotriazole (Compound XP-27) to SARS-CoV M^{pro} (Complex 1)

Complex 1 was obtained by soaking crystals of (ΔSer1/C-His_6)-SARS-CoV M^{pro} at pH 6.5 with 5 mM 1-(benzoyloxy)-benzotriazole (XP-27). The plate-like crystals displayed space group $P2_1$

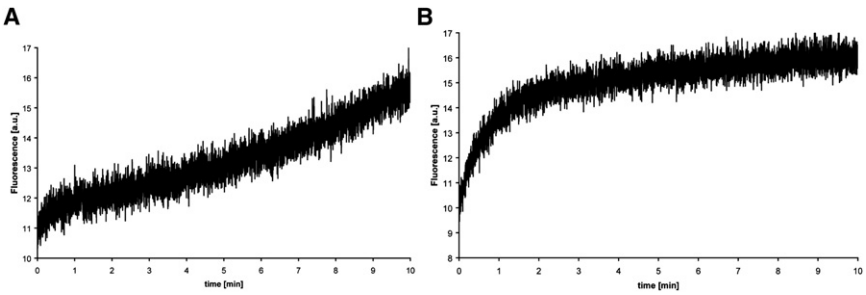

Figure 3. Inhibition Kinetics of Benzotriazole Esters

Inhibition kinetics of benzotriazole esters XP-27 (A) and XP-59 (B). The graphs show the fluorescence (in arbitrary units) created by substrate cleavage as a function of time. For inhibitor XP-27, the curve initially reaches a plateau, but after about 3–4 min, enzymatic activity seems to be restored (A). For XP-59, the expected hyperbolic curve is observed (B).

(Table 1) and contained one M^{pro} dimer in the asymmetric unit. One monomer of the dimer (protomer A) was found to be in the active conformation, whereas the other exhibits an inactive conformation in which the loop forming the oxyanion hole (residues 138–145) has a catalytically incompetent shape. This has previously been observed in other SARS-CoV M^{pro} structures when the crystals had been grown at pH 6.0–6.5, and we have postulated that the inactive form in the dimer arises when a histidine residue (His163) at the bottom of the S1 specificity pocket is protonated at low pH, leading to a reorientation of Glu166 and to the collapse of both the S1 pocket and the oxyanion hole (Yang et al., 2003; Tan et al., 2005; Anand et al., 2005; see, for instance, Protein Data Bank [PDB] ID code: 1UJ1).

Table 1. Statistics of Data Collection and Processing, and Crystallographic Refinement

	XP-27	XP-59
Data Collection		
Space group	$P2_1$	C2
Unit cell dimensions		
a (Å)	52.23	108.27
b (Å)	97.76	81.97
c (Å)	67.71	53.42
β (°)	103.01	104.3
Wavelength (Å)	0.8157	0.8080
Resolution range (Å)	40–2.25	65–1.95
Outer shell (Å)	2.34–2.25	2.02–1.95
Unique reflections	31,491	30,270
Mean redundancy[a]	3.2 (3.2)	3.4 (3.4)
Completeness (%)[a]	99.7 (100.0)	97.4 (96.8)
R_{merge} (%)[a,b]	7.3 (46.6)	12.3 (44.5)
$I/\sigma(I)$	12.9 (1.91)	12.8 (2.49)
Refinement		
R factor (%)[c]	18.30	16.48
Free R factor (%)[d]	25.59	21.01
Root-mean-square deviations from ideality		
Bonds (Å)	0.016	0.016
Angles (°)	1.57	1.64

[a] Values in parentheses are for the highest resolution shell.

[b] $R_{merge} = \sum_{hkl}\sum_i|I - <I>|/\sum_{hkl}\sum_i I \times 100\%$, where I and $<I>$ are the ith observed intensity and average intensity of the reflection hkl, respectively.

[c] R factor = $\sum_{hkl}||F_{obs}| - |F_{calc}||/\sum_{hkl}|F_{obs}| \times 100\%$.

[d] Free R factor = $\sum_{hkl<T}||F_{obs}| - |F_{calc}||/\sum_{hkl<T}|F_{obs}| \times 100\%$, where $hkl < T$ represents the test data set of 5% of the diffraction data.

When examining the electron density for monomer B, extra density was seen connected to the active-site Cys145 into which we could model a covalently bound benzoyl ester, with an occupancy of 70% (Figure 4A). The benzene ring of the inhibitor lies like a lid on top of the entrance to the S1 pocket and pushes away the Glu166 side chain, which is originally (30% occupancy remaining for this conformation) blocking the pocket. The Oε2 atom of the reoriented Glu166 now makes a hydrogen bond to the Nε2 atom of His172 (2.54 Å), just like in the active conformation (Tan et al., 2005). Presumably, the highly reactive and relatively small inhibitor induces this conformation upon binding, but its steric demands on the oxyanion loop are too limited to force this segment into the active conformation. The benzene ring of the covalently bound inhibitor makes van der Waals contacts with the rim of the collapsed oxyanion loop (Cα atoms of Asn142 and Gly143).

Surprisingly, the immediate active site of monomer A is empty and contains no electron density for a covalently bound product. However, in the hydrophobic S2 specificity pocket, we found clear difference density (>4σ) for a benzoic acid molecule. The molecule is sandwiched between the side chains of Met49 and Met165. The latter adopts two conformations, one of which (occupancy 50%) is not compatible with the presence of benzoic acid at this site. The occupancy of the benzoic acid molecule was fixed at 30%. The observation of this molecule in the S2 site immediately raises the question as to which mechanism was at work here. We assume that the thioester formed between the benzoyl group and Cys145 (with 1-hydroxybenzotriazole being the leaving group) is attacked by one of the numerous water molecules in the substrate-binding site. This results in the production of benzoic acid and restoration of the free active-site cysteine. Because of its overall hydrophobicity, the benzoic acid then binds to the nearby S2 pocket (Figure 4B). This interpretation is in full agreement with the observed biphasic kinetics for XP-27 (Figure 3A). However, even though benzoic acid itself is not an inhibitor of the enzyme up to μM concentrations (data not shown), we cannot exclude that the compound bound to the S2 pocket might originate from degradation of free XP-27 in solution over the time of the crystal-soaking experiment. In any case, our findings help explain the observation of Wu et al. (2006) that their benzotriazole inhibitors, although displaying nanomolar K_i values, did not lead to complete inhibition of the enzyme.

If hydrolysis of the enzyme-bound thioester occurs with XP-27, why then only in the A monomer? Only in this molecule is the oxyanion loop in the correct conformation to stabilize the tetrahedral intermediate of the hydrolysis reaction. In the B monomer, this loop is in the catalytically incompetent

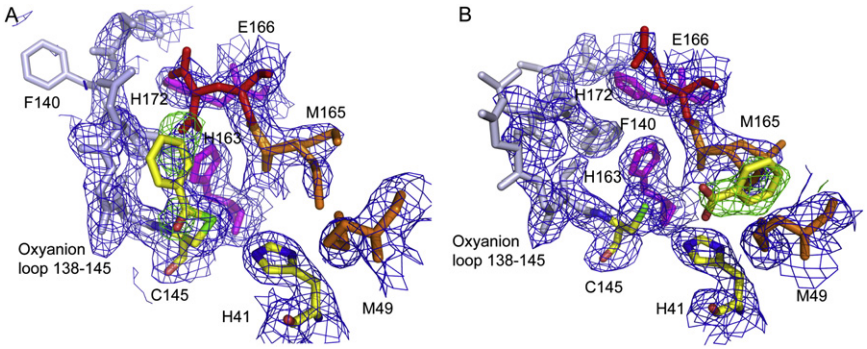

Figure 4. Active-Site Environment of the SARS-CoV M^{pro} Reacted with 1-(Benzoyloxy)-Benzotriazole

Active-site environment of the SARS-CoV M^{pro} reacted with 1-(benzoyloxy)-benzotriazole (XP-27), with corresponding $2F_o - F_c$ electron density map (contoured at 1σ above the mean).

(A) Monomer B with Cys145 acylated by the 1-(benzoyloxy) moiety (70% occupancy; atom colors), which covers the S1 specificity pocket. An $F_o - F_c$ omit map (green), contoured at 2.75σ above the mean, is shown for the inhibitor moiety. Glu166 (red) has a double conformation, one of which exists in the 30% of the molecules that do not have the active-site cysteine acylated. Met49 and Met165 (double conformation) (orange) line the S2 specificity pocket. His163 and His172 are colored in magenta. The catalytic dyad residues (Cys145 and His41) are colored by atom (yellow, carbon; red, oxygen; blue, nitrogen; green, sulfur). Loop 138–145 is in an inactive conformation (Phe140 turned away from His163) and colored gray.

(B) Monomer A represents the structure after hydrolysis of the thioester. The resulting benzoic acid molecule (atom colors; $F_o - F_c$ omit map, contoured at 2.75σ, shown in green) has entered the S2 pocket and is sandwiched between Met49 and Met165 (orange). The latter has two conformations, one of which exists only in the 50% of the molecules that do not have the benzoic acid bound. The oxyanion loop (gray) is in an active conformation, with Phe140 stacking against His163 (magenta). The $2F_o - F_c$ electron density maps (blue) are contoured at 1σ above the mean.

conformation and, therefore, the thioester adduct remains relatively stable (even though the occupancy is only 70%).

Amputation of the N Finger in (ΔSer1)/C-His$_6$ M^{pro} Leads to Local Structural Changes

Apart from some small differences, mostly in flexible loops at the periphery of the protein and at the C terminus, the dimeric structures seen in the enzyme modified by XP-27 and the original 1UJ1 dimer (Yang et al., 2003) overlay quite well. The overall root-mean-square deviation for 577 out of 600 Cα atoms is 0.36 Å. Interestingly, we found electron density for three DMSO molecules, which must originate from the DMSO used to dissolve the inhibitor in the crystal-soaking experiment. One of them fills a hole at the site where the N fingers of the two polypeptide chains approach each other, near the carbonyl groups of the Lys5 residues of both the A and the B monomer, that is, more or less on the noncrystallographic two-fold axis of symmetry (near the position where the magenta and green polypeptide segments meet in Figure 1). This site could be of interest for designing dimerization inhibitors. The two remaining DMSO molecules fill the space between the M^{pro} dimers adjacent to the crystal contacts, next to the AspB244…His#A134 (DMSO2) and the GlnA256…Trp#A31/Ala#A70 (DMSO3) contacts (# marks a residue in a symmetry-related dimer).

Because of the cloning procedure used in the present study, the N-terminal serine has been replaced by a formylmethionine which, favored by the penultimate residue being a glycine, was cleaved off during synthesis in *E. coli* (Hirel et al., 1989). This causes the "amputated N finger" (residues 2–7, ΔSer1) to become more flexible. As a result, residues Gly2 and Phe3 in both monomers A and B have flipped their orientation such that the N terminus of Gly2 is now, at least in protomer B, hydrogen bonded to the Sγ atom of Cys300 (domain III) of the parent monomer (at 2.39 Å in protomer B, 4.50 Å in protomer A) and the N finger can no longer stabilize the loop (residues 138–145) forming the oxyanion hole of the other monomer. This is observed in monomer B, where the oxyanion loop is in a collapsed conformation as discussed before. Yet, in monomer A, this loop is in the catalytically competent form although the main-chain conformation of Phe140 is no longer stabilized by the N finger of monomer B. But the phenyl ring of this residue is still embedded in a hydrophobic pocket consisting of Val114, Ala116, Tyr126, Tyr161, His163, and His172. The lack of an intact N finger, however, does make the loop 138–145 more flexible. This is reflected in the B factors of the main-chain atoms of the loop in monomer A (44.4–74.0 Å^2, with an average of 64.3 Å^2), which are higher than the average B factor of the entire main chain (40.4 Å^2). This situation is comparable to the B factors observed in the loop 138–145 of the B monomer (47.1–77.8 Å^2, with an average of 67.9 Å^2; the average B factor for the entire main chain is 41.7 Å^2). The high flexibility of the oxyanion-binding loop explains the fact that k_{cat} for the enzyme with the amputated N finger is significantly lower (40.3 min^{-1}) than for the authentic M^{pro} (1105 min^{-1}). On the other hand, deletion of the N-terminal serine may create more space in the substrate-binding site, hence the lower K_M for the (ΔSer1)/C-His$_6$ enzyme.

We have shown in this work that deletion of Ser1, Phe305, and Gln306, plus the C-terminal attachment of a hexahistidine tag (not seen in the electron density maps), reduces enzymatic activity (k_{cat}/K_M) by ≈59%. In another study, Hsu et al. (2005a) have shown that a deletion of the three N-terminal amino acid residues reduces the enzyme's activity by a mere 24%, whereas the fourth residue, arginine, is absolutely essential for catalytic activity and important for the formation of the dimer. In agreement with this, we previously reported almost total inactivation of the homologous main proteinase from TGEV upon removal of five residues from the N terminus (Anand et al., 2002). In another report, removal of the seven N-terminal residues abolishes the enzymatic activity of the main proteinase almost completely, but does not seem to have much influence on dimer formation (Chen et al., 2005a) (however, the enzyme used in this study had both N- and C-terminal extensions). It has been suggested by molecular dynamics simulations that a different dimer could form under these conditions, which involves much more elaborate contact between domains III of the monomers (Chen et al., 2005a). This would be in agreement with the observed

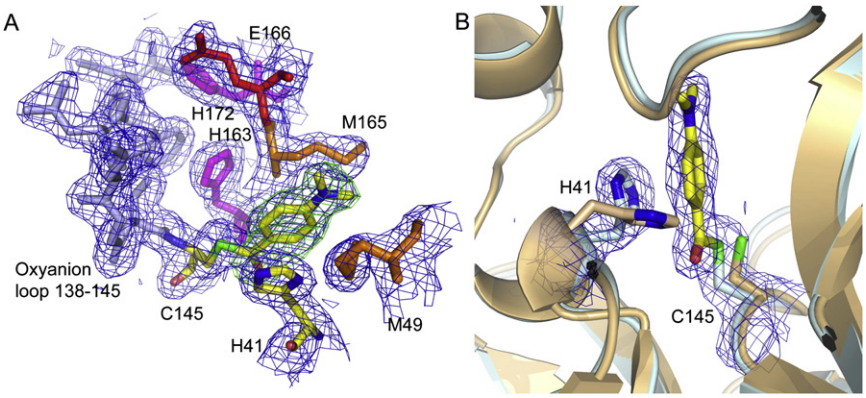

Figure 5. Active-Site Environment of the SARS-CoV M^{pro} Reacted with 1-(4-Dimethylaminobenzoyloxy)-Benzotriazole

Active-site environment of the SARS-CoV M^{pro} reacted with 1-(4-dimethylaminobenzoyloxy)-benzotriazole (XP-59), with corresponding $2F_o - F_c$ electron density map (contoured at 1σ above the mean).

(A) Cys145 is acylated by the 1-(4-dimethylaminobenzoyloxy) moiety (atom colors; color code as in Figure 4), which extends toward the S2 specificity pocket. An $F_o - F_c$ omit map (green), contoured at 2.75σ above the mean, is overlaid onto the inhibitor moiety. Met49 and Met165 (orange) line the S2 specificity pocket. His163 and His172 are colored in magenta. The catalytic dyad residues (Cys145 and His41) are colored by atom. Loop 138–145 is in an active conformation and colored gray. The $2F_o - F_c$ electron density map is contoured at 1σ above the mean.

(B) Comparison of the active site of the free enzyme (light orange) with the 1-(4-dimethylamino)-benzoyl thioester (gray). $2F_o - F_c$ electron density (contoured at 1σ above the mean) is shown for the thioester and His41. The latter has rotated in comparison to the free enzyme and is now stacking against the aromatic moiety of the inhibitor.

dimerization of isolated domain III of SARS-CoV M^{pro} (Shi et al., 2004). Although the N-terminal residues obviously have an effect on the stability of an intact substrate-binding site, the catalytic activity of the M^{pro} is probably mainly controlled by the protonation states of the two histidine residues, His163 and His172, in the substrate-binding site. Molecular dynamics calculations performed on the M^{pro} dimer have emphasized the role played by these two histidines in maintaining the correct conformation of the substrate-binding site (Tan et al., 2005).

Binding of 1-(4-Dimethylaminobenzoyloxy)-Benzotriazole (XP-59) to SARS-CoV M^{pro} (Complex 2)

Complex 2 was obtained by cocrystallization. SARS-CoV M^{pro} (with authentic chain termini) was incubated for 2 hr at 25°C with a 7-fold excess of 1-(4-dimethylaminobenzoyloxy)-benzotriazole (compound XP-59), and crystal growth was initiated by microseeding using crushed crystals of the free enzyme. Small block-sized (0.2 mm × 0.1 mm × 0.1 mm) crystals appeared overnight and displayed monoclinic space group C2 (Table 1), isomorphous to the crystals of the free enzyme (Xue et al., 2007). These crystals, grown at pH 6.0, have one monomer in the asymmetric unit, which has the substrate-binding site in the active conformation. Formed by the crystallographic two-fold axis from the monomer, the dimer is very similar to the one in the $P2_1$ crystal structures, except for the oxyanion loops of both monomers being in the active conformation. The largest differences occur between the C termini of the monomers and between the oxyanion loops of monomer B, which is in the collapsed conformation in the $P2_1$ crystal structure. The C terminus in the C2 crystal structure is completely visible and extends in a direction different from the apparently flexible C terminus in the $P2_1$ crystal structure. The root-mean-square deviation for 584 out of 603 Cα atoms with the dimer observed in space group $P2_1$ (Yang et al., 2003; PDB ID code: 1UJ1) is 0.83 Å, whereas this value is only 0.23 Å (297 out of 306 Cα pairs) for the comparison with the enzyme with authentic chain termini that was crystallized in space group C2 (Xue et al., 2007).

Upon inspection of the active site of the M^{pro}-inhibitor complex, clear electron density was observed for the 1-(4-dimethylamino)-benzoyl moiety covalently bound to Cys145 (Figure 5A). Surprisingly, the side chain of the other catalytic dyad residue His41 has undergone a rotation away from Cys145 (Figure 5B). It is now stacked against the phenyl ring of the inhibitor, making good π-π interactions (distance between the planes is 3.4 Å). The S1-binding pocket is not occupied by the inhibitor. Instead, a chain of three water molecules with well-defined density connects the His163 Nε2 atom at the bottom of the S1 specificity site with the side chains of Glu166 (Oε1) and Asn142 (Oδ1). The dimethylamino moiety of the inhibitor is situated between the side chains of Met49 and Met165, where it partly occupies the S2 specificity pocket. It is also involved in van der Waals interactions with the main-chain atoms of residues Asp187, Arg188, Gln189, and Pro39. A similar binding mode of the inhibitor to the main proteinase is observed when C2 crystals of the free enzyme are soaked at pH 7.0 with a 20-fold excess of compound XP-59 (data not shown). Binding of a substituted phenyl group to the S2 specificity subsite has also been observed in other studies (e.g., Goetz et al., 2007).

In the crystal structure of complex 2, the loop 138–145 is being held in the active conformation by the N finger of the symmetry-related molecule (distance SerB1 N–PheA140 O: 2.67 Å) in order to create the perfect environment for the oxyanion transition state. The conformation of this loop is quite stable, as can be deduced from the B factors of the main-chain atoms of the loop compared to the overall B factor of the entire main chain (ranging from 24 to 34 Å^2 with an average of 28.6 Å^2, compared to 31.5 Å^2). Equally, the amino terminus of the N finger is also hydrogen bonded to Glu166 Oε1 (at 2.75 Å), preventing closure of the S1 specificity pocket by the Glu166 side chain. This catalytically competent conformation explains the high k_{cat} (1105 min^{-1}) observed for the authentic enzyme, when compared to the situation in the enzyme featuring the amputated N finger ([ΔSer1]/C-His_6; k_{cat} = 40.3 min^{-1}).

Comparison of the crystal structures of the two M^{pro}-inhibitor complexes shows that the covalently bound suicide-inhibitor products are oriented in different directions (cf. Figures 4A and 5A). The benzoyloxy moiety in complex 1 (molecule B) is covering the S1 specificity pocket (Figure 4A), whereas the dimethylamino

group in complex 2 is entering the S2-binding site (Figure 5A). In an attempt to explain how the inhibition can proceed, Wu et al. (2006) have modeled a number of their benzotriazole inhibitors, among them XP-59, into the active site of the SARS-CoV M^{pro}. In their model of the Michaelis complex, the benzotriazole is positioned in the oxyanion hole environment and the remainder of the inhibitor is located in the vicinity of amino acid residues Thr25, Thr26, His41, Thr45, Ala46, and Met49, leaving the carbonyl group of the benzotriazole ester close enough to the $S\gamma$ of the active-site Cys145 for a nucleophilic attack to occur. This orientation of the inhibitor is possible, but then the resulting covalently bound products have to swing at least 90° around the covalent bond to occupy an energetically probably more favorable niche on top of the S1-binding site or in the S2 pocket in the two crystal structures, respectively. Because of the rather small size of the products of suicide inhibition, this should be possible without serious steric clashes. That structural rearrangements must have happened in the enzyme after the reaction with the inhibitor is clear in the crystal structure of M^{pro} complexed with the dimethylaminobenzoyloxy moiety (from compound XP-59) where, first, the oxygen atom proposed to be stabilized in the oxyanion hole (formed by the main-chain amides of Gly143 and Cys145) during the transition state of the reaction is flipped away and makes no specific contacts anymore and, second, the side chain of the active-site residue His41 has moved away from its original position to make the stacking interactions with the inhibitor product as discussed previously (Figure 5B).

SIGNIFICANCE

Caused by a newly identified coronavirus, SARS-CoV, severe acute respiratory syndrome (SARS) is an emerging disease that has the capacity to become a global threat to world health because of its rapid transmission. The animal reservoir for the virus (most probably bats) is still existent and a renewed zoonotic transition to man cannot be excluded. Therefore, efficient drugs are needed in order to be prepared for a possible future outbreak. The SARS-CoV main proteinase (M^{pro}) plays a central role in the formation of the viral replicase/transcriptase complex and is thus an ideal target for the development of suitable drugs.

The structures of complexes of the M^{pro} resulting from reaction with two aromatic benzotriazole esters provide a promising starting point for designing more specific inhibitors for the proteinase. Because of their high reactivity, the inhibitors presented here might not be very selective, although it is encouraging to note that in the entire main proteinase with its 12 cysteine residues, only the active-site Cys145 is acylated. Furthermore, Wu et al. (2006) reported that these compounds are not cell toxic, at least not up to a concentration of 100 μM. Starting from these lead structures, the inhibitors can now be modified by substituents occupying the S1 and S2 specificity pockets in order to improve their potency and specificity. The structures presented here also demonstrate that electron-donating substituents in the benzoyl moiety are useful to stabilize the thioester bonds with the active-site cysteine against hydrolysis. Finally, the structure of the M^{pro} featuring an amputated N finger (residue Ser1 deleted) explains the reduced catalytic activity of this species.

EXPERIMENTAL PROCEDURES

Expression and Purification

The C-terminally His_6-tagged SARS-CoV M^{pro} was cloned and overexpressed in *E. coli* BL21 (DE3) cells. Plasmid pET-SCoV-Mpro-Δ305-306(6× His) was kindly provided by Dr. J. Ziebuhr. In this plasmid, the nucleotides coding for the C-terminal residues Phe305 and Gln306 have been replaced by a hexahistidine tail, whereas the codon for the N-terminal Ser1 was replaced by a start codon. Most likely, the resulting N-formylmethionine has posttranslationally been cleaved off by the methionine-aminopeptidase during expression in *E. coli* (Hirel et al., 1989). Edman degradation showed the polypeptide chain to begin with residue Gly2. The overexpressed protein was purified by nickel-NTA affinity chromatography followed by a gel-filtration step. Only the middle fractions of the resulting elution peak were pooled and used for crystallization experiments.

The plasmid coding for SARS-CoV M^{pro} with authentic N and C termini was a gift from Prof. Z. Rao (Xue et al., 2007). The plasmid was transformed in *E. coli* BL21 (DE3) cells as an N-terminal GST fusion protein with a C-terminal tag of eight extra residues containing a glycine, a proline, and six histidines (GPH_6). Because of the construction of the plasmid, the GST tag was cleaved off by autocatalytic processing of the active M^{pro}. The C-terminally GPH_6-tagged product was subjected to nickel-NTA affinity chromatography and concentrated in PreScission cleavage buffer (Walker et al., 1994). The PreScission protease cleaved off the C-terminal GPH_6 tag, producing an authentic SARS-CoV M^{pro}. The wild-type protein was further purified using anion-exchange chromatography (Xue et al., 2007).

Preparation of Benzotriazole Esters

To a stirred solution of 2.5 mmol N-hydroxybenzotriazole and 2.75 mmol triethylamine in 4 ml dichloromethane (DCM) at room temperature, 2.5 mmol benzoyl chloride was slowly added. The reaction mixture was stirred for 2 hr, diluted with DCM (20 ml), washed with saturated $NaHCO_3$ solution (2 × 4 ml) and brine (1 × 5 ml), dried over $MgSO_4$, and filtered. The solvent was removed under reduced pressure and the residue was purified to provide the desired benzotriazole.

1-(Benzoyloxy)-Benzotriazole (XP-27)

After the reaction mixture had been worked up, the crude product was purified by column chromatography using diethyl ether:cyclohexane (2:3). 1-(benzoyloxy)-benzotriazole was obtained in 91% yield as a white solid. Melting point 74°C; ms (ESI) m/z = 239.0 $[M]^+$, 105.0 $[C_6H_5CO]^+$.

1-(4-Dimethylaminobenzoyloxy)-Benzotriazole (XP-59)

After the reaction mixture had been worked up, the crude product was recrystallized from hexane:ethyl acetate. 1-(4-dimethylaminobenzoyloxy)-benzotriazole was obtained in 80% yield as a slightly yellow solid. Melting point 153°C; ms (ESI) m/z = 869.3 $[3M + Na]^+$, 587.2 $[2M + Na]^+$, 305.1 $[M + Na]^+$.

Enzyme Kinetics

Both a fluorescence-based and an HPLC assay were used to assess the activity of the SARS-CoV M^{pro}. The former made use of the fluorogenic peptide substrate Dabcyl-KTSAVLQ↓SGFRKME-Edans (95% purity; Biosyntan GmbH, Berlin, Germany), which contains the main proteinase cleavage site (indicated by the arrow). The enhanced fluorescence due to the cleavage of this substrate as catalyzed by the enzyme was monitored at 490 nm with excitation at 340 nm, using a Cary Eclipse fluorescence spectrophotometer. The experiments were performed in a buffer consisting of 20 mM Tris-HCl (pH 7.3), 100 mM NaCl, 1 mM EDTA. Kinetic parameters K_M and k_{cat} were determined by initial-rate measurements at 25°C. The reaction was initiated by adding proteinase (final concentration 0.5 μM) to a solution containing different final concentrations of the fluorogenic peptide (10–40 μM). The initial rates were converted to enzyme activities (μmol substrate cleaved per s). Kinetic constants were derived by fitting the data to the Michaelis-Menten equation with the nonlinear regression analysis program SigmaPlot (SigmaPlot 2000, version 6.00; SPSS, Chicago, IL, USA).

The HPLC-based approach has been described elsewhere (Tan et al., 2005). Briefly, the substrate used here was the pentadecapeptide SWTSAVLQ↓SGFRKWA, which also resembles the cleavage site at the N terminus of the SARS-CoV M^{pro}, except for the two tryptophans at either side of the cleavage site replacing the P7 Ile and the P6′ Met residues. The 20 μl reaction mixture contained the inhibitor at concentrations varying from 5 to 500 μM, 1.5 μM M^{pro} dimer (diluted in 100 mM morpholinoethanesulfonic acid monohydride [MES] [pH 7.0]), and 250 μM substrate. Inhibitor and M^{pro} were incubated for 5 min at room temperature before adding the substrate. The reaction was run for 5 min at 25°C, then stopped by adding 5 μl trifluoroacetic acid (0.1%) and put on ice or stored at −20°C. The samples were centrifuged and 80 μl MES buffer (100 mM) was added. Products and substrate were separated on a reverse-phase HPLC column (Jupiter 4μ Proteo 90A, Phenomenex, Torrance, CA, USA), using a gradient of acetonitrile in 0.1% trifluoroacetic acid. The product and substrate peaks were detected at 280 nm, and IC_{50} values were determined.

Inhibition Assay

The fluorescence-based assay was also used for the determination of the inhibitor constants of the two benzotriazole compounds. These tests were performed with the untagged, authentic SARS-CoV M^{pro}. Values of K_i and k_3 (see scheme above) were calculated from plots of $1/k_{obs}$ versus 1/[I] according to Equation 1 (Equation VIII.129 of Dixon and Webb, 1979):

$$\frac{1}{k_{obs}} = \frac{1}{k_3} + \frac{K_i}{k_3} \cdot \left(1 + \frac{[S]}{K_m}\right) \cdot \frac{1}{[I]}. \quad (1)$$

To obtain the observed first-order inhibition rate constant k_{obs}, time-dependent progress curves were fitted to a first-order exponential (Equation 2; equivalent to Equation A10 of Tian and Tsou, 1982, with the addition of *D*; see below):

$$F = \left(\frac{v_0}{k_{obs}}\right) \cdot \left(1 - \exp^{-k_{obs} \cdot t}\right) + D. \quad (2)$$

F is the product fluorescence (measured in arbitrary units), v_0 is the initial velocity, *t* is time, and *D* is a displacement term to account for the nonzero emission at the start of data collection.

In the experiment, the K_i and k_3 values for the irreversible inhibitors were obtained from reactions initiated by addition of the enzyme (final concentration 0.5 μM) to 20 mM Tris-HCl buffer (pH 7.3) containing 100 mM NaCl, 1 mM EDTA, 20 μM fluorogenic substrate, and inhibitor. Four different inhibitor concentrations were tested, in at least 10-fold molar excess over the enzyme in most cases. Data from the continuous assays were analyzed with the nonlinear regression analysis program SigmaPlot.

Crystallization of the Complexes

Before crystallization, the C-terminally His_6-tagged SARS-CoV M^{pro} ([ΔSer1]/C-His_6) was dialyzed against 50 mM Tris-CH_3COOH (pH 7.5), 1 mM EDTA, 5 mM DTT and concentrated to 10 mg/ml. The protein was crystallized at 18°C by vapor diffusion using hanging drops or sitting drops. The crystallization conditions were 5% PEG 10,000, 0.1 M MES (pH 6.5), 3% ethylene glycol, 50 mM ammonium acetate (Lee et al., 2005). Plate-shaped crystals of monoclinic form appeared after 3 days to a week, sometimes accompanied by needles and irregularly shaped crystals, which turned out to belong to the tetragonal space group (see Tan et al., 2005). One of the monoclinic crystals was soaked for 4 days at 18°C in the crystallization buffer solution containing 5 mM 1-(benzoyloxy)-benzotriazole (XP-27) and 10% DMSO to increase the solubility of the inhibitor.

The untagged SARS-CoV M^{pro} with authentic chain termini, concentrated to 10 mg/ml in 50 mM Tris-HCl (pH 7.5), 40 mM NaCl, 1 mM EDTA, 5 mM DTT, was incubated for 2 hr at 25°C with a 7-fold excess of the inhibitor 1-(4-dimethylaminobenzoyloxy)-benzotriazole (XP-59) and solubilized in 8% PEG 6000, 0.1 M MES (pH 6.0), 3% 2-methyl-2,4-pentanediol (MPD). Block-shaped crystals grew overnight at 20°C in 6%–8% PEG 6000, 0.1 M MES (pH 6.0), 3% MPD, after initiation of nucleation by microseeding using crushed C2 crystals of the free enzyme.

Prior to data collection, crystals obtained from both procedures were transferred for a couple of seconds to a cryoprotectant solution containing the crystallization conditions and 30% PEG 400.

Crystallographic Data Collection and Processing, and Structure Elucidation and Refinement

Statistics of data collection, processing, and refinement are summarized in Table 1. Diffraction data were collected at 100K using monochromatic synchrotron radiation provided by beamlines X11 and X13 (EMBL and Universities of Hamburg and Lübeck, DESY, Hamburg, Germany; wavelength 0.8157 and 0.8080 Å, respectively). Intensities were measured using a MAR CCD detector. Indexing, scaling, and merging of data sets were performed using DENZO and SCALEPACK (Otwinowski and Minor, 1997). Molecular replacement and refinement were carried out using MOLREP (Vagin and Teplyakov, 1997) and REFMAC (Murshudov et al., 1997), respectively, as implemented in the CCP4 suite (CCP4, 1994). Simple bulk scaling in REFMAC was preferred over Babinet scaling because this procedure better reflected the overall Wilson B factor. The search model used for molecular replacement was either the dimer or monomer A of the crystal structure of PDB ID code 1UJ1 for the data sets of SARS-CoV M^{pro} complexed with XP-27 or XP-59, respectively. The computer graphics program Coot, implemented in the CCP4 suite, was used for interpretation of the electron density maps and model building (Emsley and Cowtan, 2004). The molecular graphics package PyMOL was used to generate the figures (DeLano, 2002).

ACCESSION NUMBERS

The atomic coordinates and structure factors, respectively, have been deposited in the RCSB Protein Data Bank under ID codes 2VJ1 and r2vj1sf (for Complex 1), and 2V6N and r2v6nsf (for Complex 2).

ACKNOWLEDGMENTS

We thank Walter Verheyen for excellent technical assistance, Arnd Petersen (Research Center Borstel) for N-terminal sequencing, and Xiaoyu Wang for discussions. This work was supported by the Sino-European Project on SARS Diagnostics and Antivirals (SEPSDA) of the European Commission (contract number SP22-CT-2004-003831), the Deutsche Forschungsgemeinschaft (Hi 611/4-1), the Sino-German Center for Promotion of Research, Beijing, and the Schleswig-Holstein Innovation Fund. R.H. thanks the Fonds der Chemischen Industrie for continuous support.

Received: July 30, 2007
Revised: April 16, 2008
Accepted: April 17, 2008
Published: June 20, 2008

REFERENCES

Al-Gharabli, S.I., Shah, S.T.A., Weik, S., Schmidt, M.F., Mesters, J.R., Kuhn, D., Klebe, G., Hilgenfeld, R., and Rademann, J. (2006). An efficient method for the synthesis of peptide aldehyde libraries employed in the discovery of reversible SARS coronavirus main protease (SARS-CoV M^{pro}) inhibitors. ChemBioChem *7*, 1048–1055.

Anand, K., Palm, G.J., Mesters, J.R., Siddell, S.G., Ziebuhr, J., and Hilgenfeld, R. (2002). Structure of coronavirus main proteinase reveals combination of a chymotrypsin fold with an extra α-helical domain. EMBO J. *21*, 3213–3224.

Anand, K., Ziebuhr, J., Wadhani, P., Mesters, J.R., and Hilgenfeld, R. (2003). Coronavirus main protease (3CL^{pro}) structure: basis for design of anti-SARS drugs. Science *300*, 1763–1767.

Anand, K., Yang, H., Bartlam, M., Rao, Z., and Hilgenfeld, R. (2005). Coronavirus main proteinase: target for antiviral drug therapy. In Coronaviruses with Special Emphasis on First Insights Concerning SARS, A. Schmidt, M.H. Wolff, and O. Weber, eds. (Basel: Birkhäuser), pp. 173–199.

Arbour, N., Day, R., Newcombe, J., and Talbot, P.J. (2000). Neuroinvasion by human respiratory coronaviruses. J. Virol. *74*, 8913–8921.

Bacha, U., Barrilla, J., Velazquez-Campoy, A., Leavitt, S.A., and Freire, E. (2004). Identification of novel inhibitors of the SARS coronavirus main protease 3CL^{pro}. Biochemistry *43*, 4906–4912.

Barretto, N., Jukneliene, D., Ratia, K., Chen, Z., Mesecar, A.D., and Baker, S.C. (2005). The papain-like protease of severe acute respiratory syndrome coronavirus has deubiquitinating activity. J. Virol. *79*, 15189–15198.

CCP4 (Collaborative Computational Project, Number 4) (1994). The CCP4 suite: programs for protein crystallography. Acta Crystallogr. D Biol. Crystallogr. *50*, 760–763.

Chen, L., Gui, C., Luo, X., Yang, Q., Gunther, S., Scandella, E., Drosten, C., Bai, D., He, X., Ludewig, B., et al. (2005b). Cinanserin is an inhibitor of the 3C-like proteinase of severe acute respiratory syndrome coronavirus and strongly reduces viral replication in vitro. J. Virol. *79*, 7095–7103.

Chen, S., Chen, L., Tan, J., Chen, J., Du, L., Sun, T., Shen, J., Chen, K., Jiang, H., and Shen, X. (2005a). Severe acute respiratory syndrome coronavirus 3C-like proteinase N terminus is indispensable for proteolytic activity but not for enzyme dimerization. J. Biol. Chem. *280*, 164–173.

Chiu, S.S., Chan, K.H., Hu, K.W., Kwan, S.W., Guan, Y., Poon, L.L., and Peiris, J.S. (2005). Human coronavirus NL63 infection and other coronavirus infections in children hospitalized with acute respiratory disease in Hong Kong, China. Clin. Infect. Dis. *40*, 1721–1729.

DeLano, W.L. (2002). The PyMOL Molecular Graphics System (Palo Alto, CA: DeLano Scientific).

Dixon, M., and Webb, E.C. (1979). The Enzymes, Third Edition (London: Longman).

Drosten, C., Günther, S., Preiser, W., van der Werf, S., Brodt, H.-R., Becker, S., Rabenau, H., Panning, M., Kolesnikova, L., Fouchier, R.A.M., et al. (2003). Identification of a novel coronavirus in patients with severe acute respiratory syndrome. N. Engl. J. Med. *348*, 1967–1978.

Emsley, P., and Cowtan, K. (2004). Coot: model-building tools for molecular graphics. Acta Crystallogr. D Biol. Crystallogr. *60*, 2126–2132.

Fan, K., Wei, P., Feng, Q., Chen, S., Huang, C., Ma, L., Lai, B., Pei, J., Liu, Y., Chen, J., et al. (2004). Biosynthesis, purification, and substrate specificity of severe acute respiratory syndrome coronavirus 3C-like proteinase. J. Biol. Chem. *279*, 1637–1642.

Fouchier, R.A.M., Hartwig, N.G., Bestebroer, T.M., Niemeyer, B., de Jong, J.C., Simon, J.H., and Osterhaus, A.D.M.E. (2004). A previously undescribed coronavirus associated with respiratory disease in humans. Proc. Natl. Acad. Sci. USA *101*, 6212–6216.

Goetz, D.H., Choe, Y., Hansell, E., Chen, Y.T., McDowell, M., Jonsson, C.B., Roush, W.R., McKerrow, J., and Craik, C.S. (2007). Substrate specificity profiling and identification of a new class of inhibitor for the major protease of the SARS coronavirus. Biochemistry *46*, 8744–8752.

Graziano, V., McGrath, W.J., Yang, L., and Mangel, W.F. (2006). SARS-CoV main proteinase: the monomer-dimer equilibrium dissociation constant. Biochemistry *45*, 14632–14641.

Hegyi, A., and Ziebuhr, J. (2002). Conservation of substrate specificities among coronavirus main proteases. J. Gen. Virol. *83*, 595–599.

Hilgenfeld, R., and Pumpor, K. (2006). Sometimes intermediates do the job. Chem. Biol. *13*, 235–236.

Hirel, P.H., Schmitter, M.J., Dessen, P., Favat, G., and Blanquet, S. (1989). Extent of N-terminal excision from *Escherichia coli* proteins is governed by the side-chain length of the penultimate amino acid. Proc. Natl. Acad. Sci. USA *86*, 8247–8251.

Hsu, M.F., Kuo, C.J., Chang, K.T., Chang, H.C., Chou, C.C., Ko, T.P., Chang, G.G., Wang, A.H., and Liang, P.H. (2005b). Mechanism of the maturation process of SARS-CoV 3CL protease. J. Biol. Chem. *280*, 31257–31266.

Hsu, W.C., Chang, H.C., Chou, C.Y., Tsai, P.J., Lin, P.I., and Chang, G.G. (2005a). Critical assessment of important regions in the subunit association and catalytic action of the severe acute respiratory syndrome coronavirus main proteinase. J. Biol. Chem. *280*, 22741–22748.

Kaeppler, U., Stiefl, N., Schiller, M., Vicik, R., Breuning, A., Schmitz, W., Rupprecht, D., Schmuck, C., Baumann, K., Ziebuhr, J., et al. (2005). A new lead for nonpeptidic active-site-directed inhibitors of the severe acute respiratory syndrome coronavirus main protease discovered by a combination of screening and docking methods. J. Med. Chem. *48*, 6832–6842.

Knowles, S.R., Phillips, E.J., Dresser, L., and Matukas, L. (2003). Common adverse events associated with the use of ribavirin for severe acute respiratory syndrome in Canada. Clin. Infect. Dis. *37*, 1139–1142.

Ksiazek, T.G., Erdman, D., Goldsmith, C.S., Zaki, S.R., Peret, T., Emery, S., Tong, S., Urbani, C., Comer, J.A., Lim, W., et al. (2003). A novel coronavirus associated with severe acute respiratory syndrome. N. Engl. J. Med. *348*, 1953–1966.

Kuo, C.-J., Chi, Y.-H., Hsu, J.T.-A., and Liang, P.-H. (2004). Characterization of SARS main protease and inhibitor assay using a fluorogenic substrate. Biochem. Biophys. Res. Commun. *318*, 862–867.

Kupfer, B., Simon, A., Jonassen, C.M., Viazov, S., Ditt, V., Tillmann, R.L., Muller, A., Matz, B., and Schildgen, O. (2007). Two cases of severe obstructive pneumonia associated with an HKU1-like coronavirus. Eur. J. Med. Res. *12*, 134–138.

Lau, S.K.P., Woo, P.C.Y., Yip, C.C.Y., Tse, H., Tsoi, H.-W., Cheng, V.C.C., Lee, P., Tang, B.S.F., Cheung, C.H.Y., Lee, R.A., et al. (2006). Coronavirus HKU1 and other coronavirus infections in Hong Kong. J. Clin. Microbiol. *44*, 2063–2071.

Lee, T.-W., Cherney, M.M., Huitema, C., Liu, J., James, K.E., Powers, J.C., Eltis, L.D., and James, M.N.G. (2005). Crystal structures of the main peptidase from the SARS coronavirus inhibited by a substrate-like aza-peptide epoxide. J. Mol. Biol. *353*, 1137–1151.

Lee, T.-W., Cherney, M.M., Liu, J., James, K.E., Powers, J.C., Eltis, L.D., and James, M.N.G. (2007). Crystal structures reveal an induced-fit binding of a substrate-like aza-peptide epoxide to SARS coronavirus main peptidase. J. Mol. Biol. *366*, 916–932.

Lindner, H.A., Fotouhi-Ardakani, N., Lytvyn, V., Lachance, P., Sulea, T., and Ménard, R. (2005). The papain-like protease from the severe acute respiratory syndrome coronavirus is a deubiquitinating enzyme. J. Virol. *79*, 15199–15208.

Lu, I.-L., Mahindroo, N., Liang, P.-H., Peng, Y.-H., Kuo, C.-J., Tsai, K.-C., Hsieh, H.-P., Chao, Y.-S., and Wu, S.-Y. (2006). Structure-based drug design and structural biology study of novel nonpeptide inhibitors of severe acute respiratory coronavirus main protease. J. Med. Chem. *49*, 5154–5161.

McIntosh, K., Dees, J.H., Becker, W.B., Kapikian, A.Z., and Chanock, R.M. (1967). Recovery in tracheal organ cultures of novel viruses from patients with respiratory disease. Proc. Natl. Acad. Sci. USA *57*, 933–940.

Murshudov, G.N., Vagin, A.A., and Dodson, E.J. (1997). Refinement of macromolecular structures by the maximum-likelihood method. Acta Crystallogr. D Biol. Crystallogr. *53*, 240–255.

Otwinowski, Z., and Minor, W. (1997). Processing of X-ray diffraction data collected in oscillation mode. Methods Enzymol. *276*, 307–326.

Peiris, J.S.M., Lai, S.T., Poon, L.L.M., Guan, Y., Yam, L.Y.C., Lim, W., Nicholls, J., Yee, W.K.S., Cheung, M.T., Cheng, V.C., et al. (2003). Coronavirus as a possible cause of severe acute respiratory syndrome. Lancet *361*, 1319–1325.

Pyrc, K., Dijkman, R., Deng, L., Jebbing, M.F., Ross, H.A., Berkhout, B., and van der Hoek, L. (2006). Mosaic structure of human coronavirus NL63, one thousand years of evolution. J. Mol. Biol. *364*, 964–973.

Schmidt, M.F., Isidro-Llobet, A., Lisurek, M., El-Dahshan, A., Tan, J., Hilgenfeld, R., and Rademann, J. (2008). Sensitized detection of inhibitory fragments and iterative development of non-peptidic protease inhibitors by dynamic ligation screening. Angew. Chem. Int. Ed. Engl. *47*, 3275–3278.

Shi, J., Wei, Z., and Song, J. (2004). Dissection study on the severe acute respiratory syndrome 3C-like protease reveals the critical role of the extra domain in dimerization of the enzyme: defining the extra domain as a new target for design of highly specific protease inhibitors. J. Biol. Chem. *279*, 24765–24773.

Sidwell, R.W., Huffman, J.H., Khare, G.P., Allen, L.B., Witkowski, J.T., and Robins, R.K. (1972). Broad-spectrum antiviral activity of virazole: 1-β-D-ribofuranosyl-1,2,4-triazole-3-carboxamide. Science *177*, 705–706.

Stockman, L.J., Bellamy, R., and Garner, P. (2006). SARS: systematic review of treatment effects. PLoS Med. *3*, e343.

Tan, J., Verschueren, K.H.G., Anand, K., Shen, J., Yang, M., Xu, Z., Rao, Z., Bigalke, J., Heisen, B., Mesters, J.R., et al. (2005). pH-dependent conformational flexibility of the SARS-CoV main proteinase (M^{pro}) dimer: molecular

dynamics simulations and multiple X-ray structure analyses. J. Mol. Biol. *354*, 25–40.

Thiel, V., Ivanov, K.A., Putics, A., Hertzig, T., Schelle, B., Bayer, S., Weißbrich, B., Snijder, E.J., Rabenau, H., Doerr, H.W., et al. (2003). Mechanisms and enzymes involved in SARS coronavirus genome expression. J. Gen. Virol. *84*, 2305–2315.

Tian, W.X., and Tsou, C.L. (1982). Determination of the rate constants of enzyme modification by measuring the substrate reaction in the presence of the modifier. Biochemistry *21*, 1028–1032.

Tsai, K.C., Chen, S.Y., Liang, P.H., Lu, I.L., Mahindroo, N., Hsieh, H.P., Chao, Y.S., Liu, L., Liu, D., Lien, W., et al. (2006). Discovery of a novel family of SARS-CoV protease inhibitors by virtual screening and 3D-QSAR studies. J. Med. Chem. *49*, 3485–3495.

Tsukada, H., and Blow, D.M. (1985). Structure of α-chymotrypsin refined at 1.68 Å resolution. J. Mol. Biol. *184*, 703–711.

Vagin, A., and Teplyakov, A. (1997). MOLREP: an automated program for molecular replacement. J. Appl. Crystallogr. *30*, 1022–1025.

van der Hoek, L., Pyrc, K., Jebbing, M.F., Vermeulen-Oost, W., Berkhout, R.J., Wolthers, K.C., Wertheim-van Dillen, P.M., Kaandorp, J., Spaargaren, J., and Berkhout, B. (2004). Identification of a new human coronavirus. Nat. Med. *10*, 368–373.

Walker, P.A., Leong, L.E., Ng, P.W., Tan, S.H., Waller, S., Murphy, D., and Porter, A.G. (1994). Efficient and rapid affinity purification of proteins using recombinant fusion proteases. Biotechnology (NY) *12*, 601–605.

Woo, P.C.Y., Lau, S.K.P., Chu, C.-M., Chan, K.-H., Tsoi, H.-W., Huang, Y., Wong, B.H.L., Poon, R.W.S., Cai, J.J., Luk, W.-K., et al. (2005). Characterization and complete genome sequence of a novel coronavirus, coronavirus HKU1, from patients with pneumonia. J. Virol. *79*, 884–895.

Wu, C.-Y., Jan, J.-T., Ma, S.-H., Kuo, C.-J., Juan, H.-F., Cheng, Y.-S.E., Hsu, H.-H., Huang, H.-C., Wu, D., Brik, A., et al. (2004). Small molecules targeting severe acute respiratory syndrome human coronavirus. Proc. Natl. Acad. Sci. USA *101*, 10012–10017.

Wu, C.-Y., King, K.-Y., Kuo, C.-J., Fang, J.-M., Wu, Y.-T., Ho, M.-Y., Liao, C.-L., Shie, J.-J., Liang, P.-H., and Wong, C.-H. (2006). Stable benzotriazole esters as mechanism-based inactivators of the severe acute respiratory syndrome 3CL protease. Chem. Biol. *13*, 261–268.

Xu, T., Ooi, A., Chen, L., Wilmouth, R., Liu, D.X., and Lescar, J. (2005). Structure of the SARS coronavirus main proteinase as an active C2 crystallographic dimer. Acta Crystallogr. *F61*, 964–966.

Xue, X., Yang, H., Shen, W., Zhao, Q., Li, J., Yang, K., Chen, C., Jin, Y., Bartlam, M., and Rao, Z. (2007). Production of authentic SARS-CoV M^{pro} with enhanced activity: application as a novel tag-cleavage endopeptidase for protein overproduction. J. Mol. Biol. *366*, 965–975.

Xue, X., Yu, H., Yang, H., Xue, F., Wu, Z., Shen, W., Li, J., Zhou, Z., Ding, Y., Zhao, Q., et al. (2008). Structures of two coronavirus main proteases: implications for substrate binding and antiviral drug design. J. Virol. *82*, 2515–2527.

Yang, H., Yang, M., Ding, Y., Liu, Y., Lou, Z., Zhou, Z., Sun, L., Mo, L., Ye, S., Pang, H., et al. (2003). The crystal structures of severe acute respiratory syndrome virus main proteinase and its complex with an inhibitor. Proc. Natl. Acad. Sci. USA *100*, 13190–13195.

Yang, H., Xie, W., Xue, X., Yang, K., Ma, J., Liang, W., Zhao, O., Zhou, Z., Pei, D., Ziebuhr, J., et al. (2005). Design of wide-spectrum inhibitors targeting coronavirus main proteases. PLoS Biol. *3*, e324.

Ziebuhr, J., Herold, J., and Siddell, S.G. (1995). Characterization of a human coronavirus (strain 229E) 3C-like proteinase activity. J. Virol. *69*, 4331–4338.

Ziebuhr, J., Snijder, E.J., and Gorbalenya, A.E. (2000). Virus-encoded proteinases and proteolytic processing in *Nidovirales*. J. Gen. Virol. *81*, 853–879.

